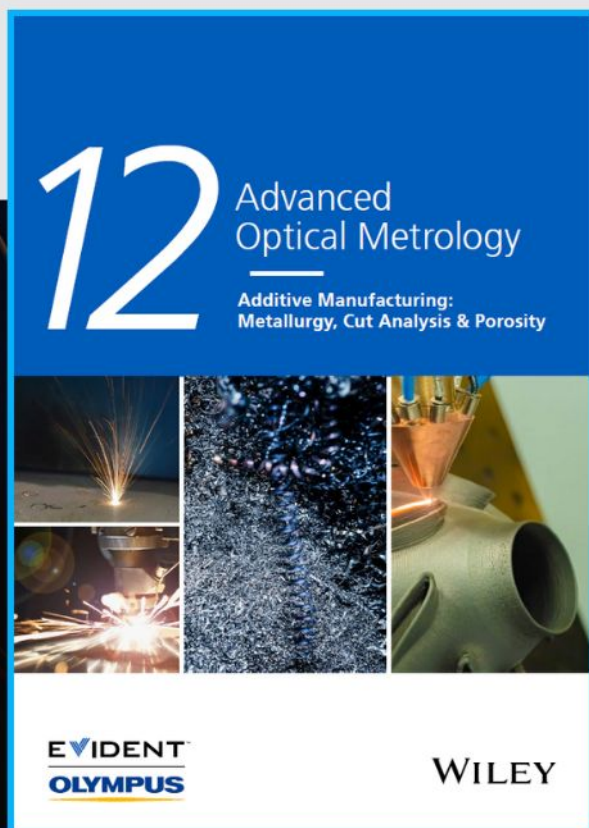




Additive Manufacturing: Metallurgy, Cut Analysis & Porosity

The latest eBook from
Advanced Optical Metrology.
Download for free.



In industry, sector after sector is moving away from conventional production methods to additive manufacturing, a technology that has been recommended for substantial research investment.

Download the latest eBook to read about the applications, trends, opportunities, and challenges around this process, and how it has been adapted to different industrial sectors.

EVIDENT™
OLYMPUS

WILEY

Roles of Nitrogen on TWIP in Advanced Austenitic Stainless Steels

Guocai Chai,* Raveendra Siriki, Joakim Nordström, Zhihua Dong, and Levente Vitos

The influence of nitrogen on the mechanical properties of two high Ni containing advanced austenitic stainless steels with low stacking fault energies is investigated. The results show that increase of nitrogen content greatly increases both strength and elongation of the steel at the same time. At the cryogenic temperature, the steels show a twin induced plasticity behavior. Ab initio calculations indicate that the increase of nitrogen slightly increases the stacking fault energy and consequently the critical shear stress for twin initiation in the steel. However, addition of nitrogen significantly increases the flow stress. This leads to a smaller critical strain for twin initiation and promotes deformation twinning in the high nitrogen steel. This is confirmed by the microstructure investigation. Deformation in steels is a competitive process between slip and twinning. Dislocation slip is dominant at low strain range, but formation of stacking fault and twinning become important in the later stages of deformation. At cryogenic temperature, it is mainly deformation twinning. The influence of nitrogen addition on magnetic property and its effect on deformation twinning are also discussed. The present study increases the understanding for the development of high-performance and low-cost advanced austenitic stainless steels.

1. Introduction

Austenitic stainless steel, due to its good combination of corrosion resistance and mechanical properties, is an ideal and versatile material for various applications.^[1,2] In the most demanding industries, special grades of austenitic stainless steels with greater corrosion resistances at different temperature ranges should be used in order to meet the requirements. These materials usually contain high amounts of Ni and Mo for a lower corrosion rate and high amounts of Cr and Mo to promote passive film formation. Despite the importance of the corrosion resistance, the strength and ductility of stainless steels are becoming a concern in many applications such as deep-water technology. Stainless steels with a combination of excellent corrosion resistance and high strength are needed. For these challenges, advanced high alloyed stainless steels have been developed.^[3]

Advanced super austenitic stainless steel

was defined as a group of austenitic stainless steels with a Ni content near or higher than 30 wt% and a pitting resistance equivalent number (PRE value) near or higher than 40.^[4] Austenitic stainless steels are inherently sensitive to chloride-induced stress corrosion cracking (SCC), which places a critical requirement for the Ni content. A good SCC resistance can be obtained only when the Ni content in the alloy is near or higher than 30%.^[5]

Nitrogen as an alloying element has been widely used in austenitic stainless steels. Addition of nitrogen offers several beneficial effects on the properties and provides a good combination of high strength, good toughness, and excellent corrosion resistance.^[6–11] Nitrogen is also a strong austenite stabilizer and can thereby replace expensive Ni in austenitic stainless steels. High nitrogen stainless steels are becoming an increasingly important new class of engineering materials with commercial importance.^[7,10,12,13]


Nitrogen is an interstitial element. Addition of nitrogen in steel alloy has the following two effects on the structure. One is to introduce strong elastic distortions into the crystal lattice. This gives rise to a strong interstitial solid solution hardening and cold deformation strengthening effects.^[14,15] Another is to cause the change of stacking fault energy^[16–18] and consequently influences the deformed microstructure.^[19] It is reported that increase of amount of nitrogen content in austenitic stainless steels increases the tendency to form planar dislocation structures.^[11] Another report shows that plastic deformation in those steels occurs by a combination of planar glide and mechanical

G. Chai, R. Siriki, J. Nordström
Research, Sandvik Materials Technology
81181 Sandviken, Sweden
E-mail: guocai.chai@sandvik.com

G. Chai, J. Nordström
Engineering Material
Linköping University
58183 Linköping, Sweden

Z. Dong, L. Vitos
Material Science and Engineering
KTH
10044 Stockholm, Sweden

Z. Dong
Material Science and Engineering
Chongqing University
400044 Chongqing, China

 The ORCID identification number(s) for the author(s) of this article can be found under <https://doi.org/10.1002/srin.202200359>.

© 2022 The Authors. Steel Research International published by Wiley-VCH GmbH. This is an open access article under the terms of the Creative Commons Attribution-NonCommercial-NoDerivs License, which permits use and distribution in any medium, provided the original work is properly cited, the use is non-commercial and no modifications or adaptations are made.

DOI: 10.1002/srin.202200359

twinning. However, the critical stress/strain conditions for the onset of mechanical twinning depend strongly on the actual nitrogen content.^[20] This phenomenon was also observed in high nitrogen Fe–Cr–Mn–Mo–N stainless steels.^[19] Planar dislocation structure is formed in the low strain region but stacking faults together with well-developed deformation twinning are formed in the high-strain regime.^[19] Recently, the deformation mechanisms in three high nitrogen-containing austenitic stainless steels were studied using both ab initio calculations and experimental investigation. The results show that large amounts of nitrogen in the steels suppress cross-slip and promote dislocation planarization, and their deformation behavior cannot be explained merely in terms of the stacking fault energy.^[21] Besides these interesting results, the following two phenomena are still not clear. One is the influence of nitrogen on stacking fault energy and its role to deformation mechanism in high nitrogen austenitic steels.^[22] It was reported that nitrogen can efficiently lower the stacking fault energy.^[16,17] Decrease in the stacking fault energy leads to a wider partial dislocation separation. A lower stacking fault energy would also increase the tendency for both formation of planar dislocation structure and nucleation of deformation twins.^[16,22] Opposite to this, it was argued that as an interstitial element, the addition of nitrogen results in lattice expansion that increases the stacking fault energy of the alloy.^[23,24] Dislocation planarization in the high nitrogen steels occurs due to the short-range ordering of nitrogen and other alloying elements. This can also suppress deformation twinning.^[23] Another important factor that is less discussed is the influence of nitrogen on the ductility of austenitic steels. Planar dislocation slip and deformation twinning have been regarded as important deformation modes in high nitrogen austenitic steels. This leads to good ductility and high toughness of the material.^[8–11] Recently, it is reported that increase in nitrogen content in the Si containing austenitic stainless steels can result in a decrease in uniform elongation.^[25] It was believed that

formation of stress concentration by planarization of dislocation causes a decrease in uniform elongation.^[26]

In this study, the influence of nitrogen on the deformation behaviors at room and cryogenic temperatures of two high Ni containing advanced austenitic stainless steels is studied experimentally and theoretically using ab initio simulation. Influence of nitrogen on deformation twinning mechanism is also discussed.

2. Experimental Section

In this study, two advanced austenitic stainless steels were manufactured. **Table 1** shows the chemical compositions of the alloys. The alloys have similar amounts of the alloying elements, except significant variation in the nitrogen contents. Alloy 27 has 0.051 wt% of nitrogen, while Alloy 34 has 0.24 wt% nitrogen. The materials used in this study were Ø50 mm hot extruded bar solution annealed at temperatures between 1150 and 1200 °C. However, they have different grain structures as shown in **Figure 1**. The grain size of Alloy 27 is about 95 µm, and Alloy 34 has a grain size of 261 µm. These grains contain plenty of annealing twins, but almost without any preferred crystallographic orientation/texture.

The samples for the tensile testing were taken in the longitudinal direction of the bar materials. The tensile testing was carried out in two different tensile test machines: a Roell–Korthaus (air) and an Instron 5982 (cryogenic temperature). Round specimens with a diameter of 5 mm and a gauge length of 50 mm were used in accordance with ASTM E8. The tensile testing was carried out with an initial strain rate of $8 \times 10^{-4} \text{ s}^{-1}$ and changed to $5 \times 10^{-3} \text{ s}^{-1}$ at the technological strain corresponding to 0.044. The tensile tests were performed at two different temperatures: room temperature (RT) (25 °C) and the cryogenic

Table 1. Chemical composition of the hot extruded alloys (wt%).

Alloys	C	Si	Mn	Cr	Ni	Mo	Cu	N	Fe	PRE value ^{a)}
27	0.012	0.49	3.63	26.28	31.2	3.21	0.96	0.051	bal.	38
34	0.009	0.49	3.58	26.22	31.46	3.24	0.98	0.24	bal.	41

^{a)}PRE value = Cr + 3Mo + 16N.

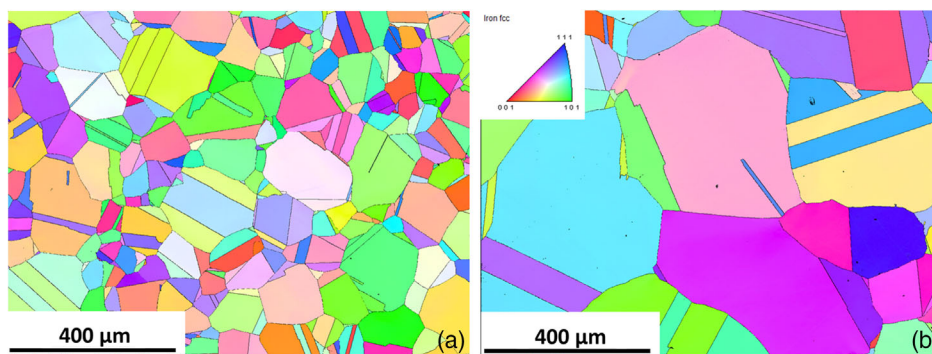


Figure 1. EBSD orientation maps on the heads of the tensile specimens along the tensile direction in the as-received condition, (a) Alloy 27 and (b) Alloy 34.

temperature (CT) of liquid nitrogen (-196°C). Three replicates were run at both temperatures.

The microstructure was investigated using a Carl Zeiss SIGMA FEG-SEM equipped with a symmetry electron backscatter diffraction (EBSD) detector supplied by OXFORD Instruments. EBSD measurements were carried out with an accelerating voltage of 20 keV, aperture size of $120\text{ }\mu\text{m}$, and scanning step size of $0.5\text{ }\mu\text{m}$. With the EBSD technique, grain structure and deformation twins were studied. The postprocessing of the EBSD data was performed in CHANNEL5 data processing software with the Tango module from OXFORD Instruments. The deformation structures (dislocation slip, stacking fault, and deformation twin) were studied using electron channel contrast image (ECCI) technique in a FIB SEM with FEG tip manufactured by Carl Zeiss. ECCI measurements were performed by collecting backscattered electron (BSE) images at an accelerating voltage of 10 keV and aperture size of $120\text{ }\mu\text{m}$. It should be noted that both the SEMs used in this study are equipped with Gemini Column technology. To obtain good results, samples were subjected to polishing with colloidal silica in the final step.

Magnetic properties were evaluated using a Quantum Design Magnetic Property Measurement System (MPMS-XL). Magnetization versus temperature relations were studied in a magnetic field of 0.05 T . The measurement started by warming up the sample to 370 K , applying the field, and then measuring the magnetization down to 5 K in steps of 5 K interval.

3. Ab Initio Calculation on Stacking Fault Energy

Generalized stacking fault energies (GSFE) of the alloys were calculated using the ab initio alloy theory. The intrinsic stacking fault energy (γ_{isf}), unstable stacking fault energy (γ_{usf}), and unstable twinning fault energy (γ_{utf}) were calculated by using a supercell approach as in our^[27–29] earlier works. The one-electron Kohn–Sham equations were solved within the framework of exact muffin-tin orbitals (EMTO) method.^[30–34] The scalar-relativistic approximation and the soft-core scheme were applied. The self-consistent electronic structure calculations and the total energy calculations were performed based on the

generalized gradient approximation.^[35] The chemical disorder and the magnetic disorder in the steels were described using the coherent potential approximation^[36,37] in combination with the disordered local moment scheme.^[38–41]

The stacking fault energy (γ) values were calculated at ambient (298 K) and cryogenic (77 K) conditions. The thermal effect was included by accounting for thermal lattice expansion and the associated magnetic contribution. The lattice parameter at ambient temperature was determined by using X-ray diffraction measurement for the alloys. They are similar to that derived from the expression established in ref. [42], where the alloying effect including nitrogen is considered. The thermal expansion coefficient^[43] was then used to determine the lattice parameter at the cryogenic temperature. In view of the relatively low magnetic transition temperature of austenitic steels,^[44] the γ values were calculated in the paramagnetic (PM) state at 298 K , while in both the PM and ferromagnetic (FM) states at 77 K for comparison. Based on the computed intrinsic energy barriers, the critical twinning stress (τ_{ctss}) representing the smallest shear stress required to nucleate twins upon plastic deformation is evaluated by using the model proposed in refs. [45,46].

4. Results

4.1. Tensile Deformation Behavior

Figure 2 shows three types of tensile test curves of Alloy 27 and Alloy 34 at RT (25°C) and liquid nitrogen temperature (-196°C)—first: engineering stress versus strain $-\sigma$ versus ϵ , then: true stress versus strain $-\sigma_{\text{true}}$ versus ϵ_{true} , and finally: strain hardening $-d\sigma/d\epsilon$ versus ϵ_{true} . Table 2 shows their

Table 2. Tensile properties of Alloy 27 and Alloy 34 at RT and -196°C .

Alloys	RT (25°C)			-196		
	$R_{p0.2}$ [MPa]	R_m [MPa]	A [%]	$R_{p0.2}$ [MPa]	R_m [MPa]	A [%]
Alloy 27	269	572	58.7	507	1018	84.0
Alloy 34	335	666	63.9	617	1220	74.7

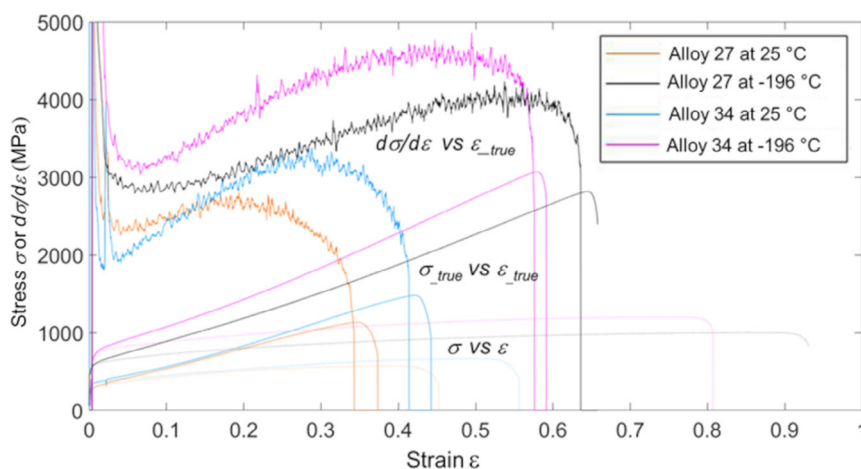


Figure 2. Tensile test curves of Alloy 27 and Alloy 34 at RT (25°C) and liquid nitrogen temperature (-196°C); engineering stress versus strain $-\sigma$ versus ϵ (dash lines), true stress versus strain $-\sigma_{\text{true}}$ versus ϵ_{true} (solid lines) and strain hardening $-d\sigma/d\epsilon$ versus ϵ_{true} (above zigzag lines).

tensile properties. At RT. Alloy 27 shows a good combination of high strength and elongation. With addition of 0.24 wt% nitrogen, Alloy 34 shows an increase of 0.2% proof strength ($R_{p0.2}$) about 24.5% and tensile strength (R_m) about 16.4%. It is not expected that Alloy 34 also shows a higher elongation (A), about 8.9% higher than that of Alloy 27. This is a novel observation, i.e., that addition of nitrogen can increase both strength and elongation simultaneously in advanced austenitic stainless steels. The strain hardening curves show that Alloy 34 has a faster increase of the strain hardening rate and finally also reaches higher strain hardening rates.

At -196°C , both alloys show even higher strength and elongation. For Alloy 27, $R_{p0.2}$ increases about 88.5%, R_m increases 78.0%, and elongation increases 43.1%. For Alloy 34, the increases of $R_{p0.2}$ and R_m are similar with those of Alloy 27, being about 84.2% and 83.2%, respectively. However, the increase of elongation is only 16.9%, which is much lower compared to Alloy 27. Hence, Alloy 27 has a higher elongation compared to Alloy 34 at -196°C as shown in both Figure 2 and Table 2, but Alloy 34 has still higher $R_{p0.2}$ and R_m due to its higher strain hardening rate during the whole strain range.

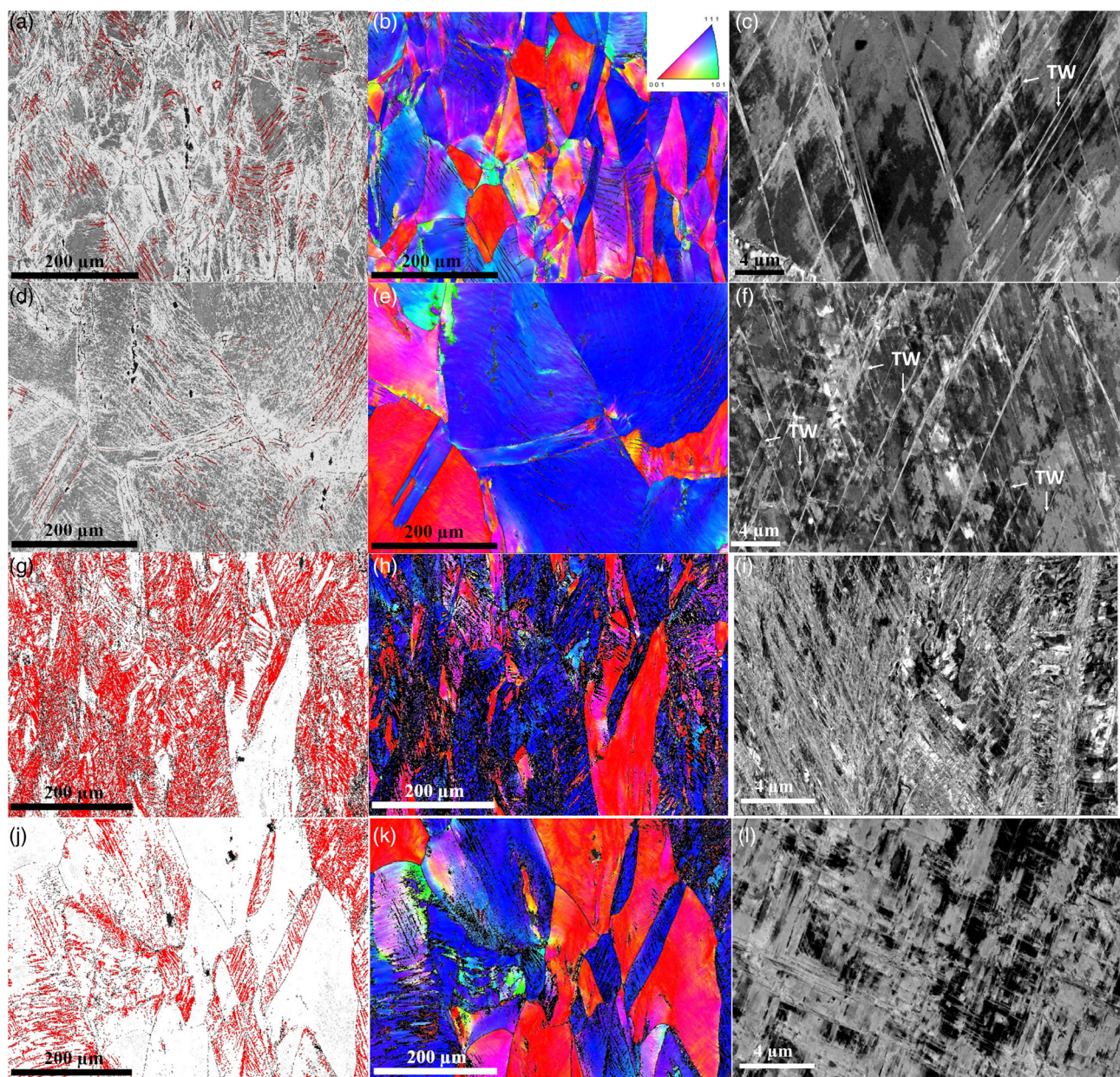


Figure 3. EBSD images of the band contrast and grain boundary maps (a), (d), (g) and (j), red lines-twins; orientation maps with respect to tensile loading direction (b), (e), (h) and (k), blue: $\langle 111 \rangle$, green: $\langle 110 \rangle$, red $\langle 001 \rangle$; and ECCL images (c), (i) of Alloy 27 and (f), (l) of Alloy 34 deformed at different temperatures and taken 3 mm from the fracture; (a–c) Alloy 27 at RT, (d–f) Alloy 34 at RT, (g–i) Alloy 27 at -196°C and (j–l) Alloy 34 at -196°C .

4.2. Deformation Microstructure

Figure 3 shows the deformation structures of Alloy 27 and Alloy 34 evaluated in SEM using EBSD and ECCI techniques. EBSD images of the band contrast and grain boundary maps show the grain structures including low angle grain boundary $<10^\circ$ (white points), high angle grain boundary $>10^\circ$ (black lines), and $\Sigma 3$ twin boundary with grain misorientation of 60° (red lines). EBSD orientation images show the crystal or grain orientations along the tensile direction. ECCI images show the deformation structures and the observed lines are deformation twins.

The images of the band contrast images show that dislocation slip and deformation twinning have occurred in both Alloy 27 and Alloy 34 at room temperature (Figure 3a,d). Deformation twinning mainly occurred in the $<111>$ grains along the tensile loading and no such deformation twins can be observed in $<100>$ grains (Figure 3b,e). The twinning in $<111>$ grains of FCC steels subjected to tensile testing at room temperature is well reported.^[13,41,47,48] The volume fraction of $\Sigma 3$ twin boundary in Alloy 27 is 5.08% but only 2.84% in Alloy 34. However, the ECCI images show that more fine deformation twins with multiple twin systems can be observed in Alloy 27 (Figure 3c) and especially in Alloy 34 (Figure 3f). These fine twins may not be evaluated by EBSD due to its resolution limitation. This indicates that the quantified twinning fraction from EBSD does not account for the observed nanodeformation twins in the ECCI images.

At -196°C , dense deformation twins can be observed in both alloys (Figure 3g,j). The volume fraction of $\Sigma 3$ twin boundary in Alloy 27 is now 16.9% but 6.39% in Alloy 34, which are much more than those in the samples tested at RT. The ECCI images (Figure 3i,l) show that these twins are also much finer and with multitwin systems. However, Alloy 34 has less twin density and more low-angle grain boundaries or stress concentration areas (Figure 3j). There are also some grains where no or few deformation twins can be observed. With inverse orientation image along the tensile loading direction, they are $<100>$ grains (Figure 3h,k). Alloy 34 has more such oriented grains than the Alloy 27.

4.3. Stacking Fault Energy

As shown in Table 3, both Alloy 27 and Alloy 34 exhibit relatively low γ_{isf} in the PM state. The increased nitrogen content in Alloy 34 leads to slightly increased γ_{isf} and decreased γ_{usf} and γ_{utf} at the given temperatures. With decreasing temperature from 298 to 77 K, γ_{isf} of Alloy 27 and Alloy 34 reduces by $6\text{--}7\text{ mJ m}^{-2}$ in the PM state, while γ_{usf} and γ_{utf} increase slightly. Nevertheless, when the possible FM transition at cryogenic condition is considered, the γ_{isf} calculated in the FM state at 77 K increases to $\approx 32\text{ mJ m}^{-2}$ for Alloy 27 and Alloy 34, while γ_{usf} decreases noticeably. Namely, the magnetic state has strong influence on the stacking fault energies and the corresponding temperature dependence.

Table 3. Stacking fault energies of steel Alloy 27 and Alloy 34 at different temperatures and magnetic states. T is in units of K and the energy barriers are in mJ m^{-2} .

Alloy	T	Magnetic state	γ_{isf}	γ_{usf}	γ_{utf}
Alloy 27	298	PM	17.8	250.7	257.0
	77	PM	11.1	258.6	262.1
	77	FM	32.1	246.2	260.3
Alloy 34	298	PM	19.2	248.2	255.3
	77	PM	13.0	256.1	260.5
	77	FM	32.4	244.3	258.5

5. Discussion

5.1. Influence of Temperature on Critical Stress or Strain for Twin Initiation

In FCC metals such as austenitic steels, dislocation slip, twinning, and phase transformation can commonly occur depending on material composition, environment, and mechanical stress applied [9, 13, 40]. Stacking fault energy of the alloy plays an important role to the deformation mechanism.^[18,19,41,42,46] Meyer et al.^[48] proposed a model for the onset of twinning in metals. Plastic deformation in metals is a competitive process between dislocation slip and twinning with increasing strain. When the applied stress or flow stress is higher than that to activate dislocation initiation or that can cause a continuous deformation, deformation will be dominant by dislocation slip. However, when the applied stress or flow stress in the material is higher than the critical shear stress for twin initiation, deformation by twinning will occur.^[49] The critical twinning shear stress (τ_{ctss}) is estimated as follows^[50]

$$\tau_{\text{ctss}} = \sigma_0 + \frac{K}{\sqrt{D}} \quad (1)$$

where D represents the grain size; K is the strengthening coefficient and is unknown for the studied steels. Nevertheless, the K value of high-Mn TWIP steels was reported to be in the range from ≈ 330 to $530\text{ MPa } \mu\text{m}^{1/2}$ depending on the chemical composition.^[50–52] Here, we assumed an average K value of $430\text{ MPa } \mu\text{m}^{1/2}$ for the studied steels to include the effect of grain size on τ_{ctss} . σ_0 is the critical twinning stress corresponding to coarse grain size, i.e., $\sigma_{\text{T}} = \sigma_0$ when $D \rightarrow \infty$. By considering the equilibrium of forces acting on the individual twinning dislocation, Kibey et al.^[53] have proposed the following models to evaluate σ_0

$$\sigma_0 = \frac{1}{m} \left[\frac{5}{18b_{\text{T}}} (\gamma_{\text{utf}} + \gamma_{\text{isf}}) - \frac{4}{18b_{\text{T}}} (\gamma_{\text{usf}} + \gamma_{\text{isf}}) \right] \quad (2)$$

where m is the average Schmid factor that is taken as 0.326^[54] and b_{T} is the Burgers vector of twinning partials.

Table 4 shows that at room temperature, the critical shear stress for twin initiation, τ_{ctss} , and the critical strain for twin initiation, $\epsilon_{\text{ctss-tr}}$ in Alloy 34 is smaller than that in Alloy 27.

Table 4. Critical stress and strain for twin initiation in Alloy 27 and Alloy 34 at different temperatures and magnetic states. The critical strain values are extracted from the measured tensile curves using the theoretical critical stress values.

Alloys	T [K]	Magnetic state	σ_0 [MPa]	τ_{ctss} [MPa]	$\epsilon_{\text{ctss-tr}}$
Alloy 27	298	PM	352	396	0.247
	77	PM	337	381	0.040
	77	FM	409	453	0.095
Alloy 34	298	PM	353	380	0.222
	77	PM	339	366	0.012
	77	FM	405	432	0.032

The $\epsilon_{\text{ctss-tr}}$ is the true strain extracted from the true stress versus true strain curve using the theoretical critical stress value. Addition of nitrogen slightly increases the stacking fault energy. Nevertheless, the difference in grain size of these two alloys is large, the influence of which on the critical twinning stress is evaluated using Equation (1) and shown in Table 4. Accordingly, in combination with the grain size effect, Alloy 34 with higher N content still exhibits relatively low critical shear stress for twin initiation. Furthermore, addition of nitrogen significantly increases the flow stress, and hence decreases the critical strain for twin initiation, $\epsilon_{\text{ctss-tr}}$. This indicates that deformation twinning occurs earlier in Alloy 34 with a higher increasing rate because a steel alloy with a higher nitrogen content has a higher strengthening rate. A higher flow stress on the other hand increases twin initiation rate and amounts of twins in the material, and consequently increases the total elongation or ductility.

At the cryogenic temperature, a lower critical stress and higher flow stress will cause twin initiation at the very early deformation stage with only few percentages of deformation strain if the alloys are in the PM state. This can explain why plenty of deformation twins have formed at the cryogenic temperature, which leads to a TWIP behavior in the alloys. An interesting phenomenon is that Alloy 34 has higher flow stresses and a lower critical stress for twin initiation if the alloy remains in the PM state; however, the alloy has a lower twin density and consequently a lower elongation than that of Alloy 27. It is difficult to give a good explanation just now. Magnetic state in the alloy can be one of the reasons

because the alloy with different magnetic state has different stacking fault energy as shown in Table 3. The material with an ordered magnetic state has a higher stacking fault energy according to our calculations. They will affect the critical stress for twin initiation as shown in Table 4. This will be discussed as follows.

5.2. Influence of Temperature on Magnetic Properties

These two alloys are stable austenitic stainless steels. EBSD study shows that no phase transformation occurred after the deformation both at RT and cryogenic temperature. However, magnetic properties evaluation shows that magnetic moments (M) slightly increase with decrease of temperature, but then increase quickly at certain temperature. This critical temperature is determined by a derivative of magnetic moment versus temperature. Here, for illustration, we take the derivative of $1/M$ (which is supposed to give a temperature slightly above the true ordering or freezing temperature where a substantial magnetic short-range order can develop). The so obtained transition temperature for Alloy 34 is 93 K (-180°C) and 67 K (-206°C) for Alloy 27. We emphasize that these temperatures do not correspond to a transition from PM state to a FM state; they only indicate a marked increase in the magnetization with decreasing temperature. The true low-temperature magnetic state of these alloys is likely to be spin glass with freezing temperature far below 50 K (not shown). Nevertheless, we know from theory that magnetic ordering strongly affects the stacking fault energy. Namely, a magnetically ordered state can lead to very different GSFE surface topology as compared to the magnetically disordered state.^[55]

Due to the difficulty to quantitatively evaluate the influence of complex magnetic state like spin glass on the stacking fault energy, here the FM state is used to model a low-temperature magnetic state and illustrate the influence of magnetic transition on the stacking fault energy. As shown in Table 3, the stacking fault energies of these two alloys at -196°C are much higher in FM state than in PM state. In addition, Figure 4 shows that Alloy 34 has a relatively high magnetic transition temperature. Namely, at the testing temperature of -196°C , the magnetic order state is preferable in Alloy 34 than Alloy 27. Therefore, Alloy 34 is expected to have a higher stacking fault energy and thus critical twinning stress than Alloy 27 at -196°C .

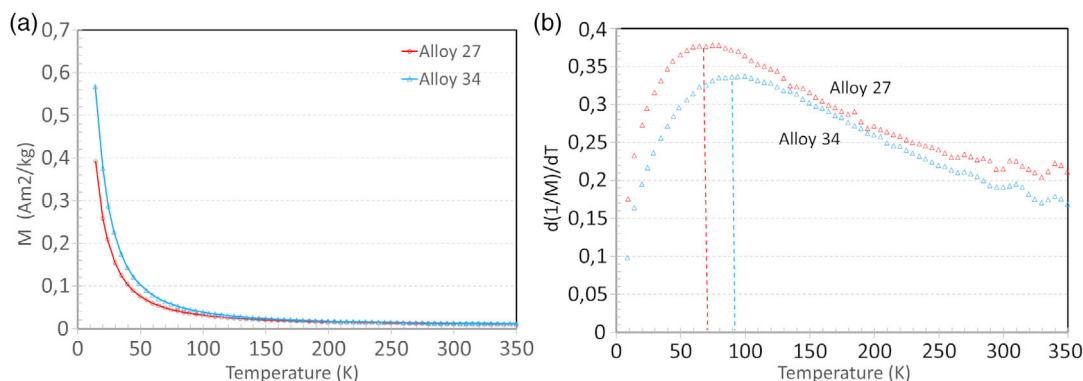


Figure 4. a) Magnetic properties evaluated by MPMS-XL. b) Magnetic moment versus temperature. Derivative of magnetic moment versus temperature.

This may cause that it is easier for Alloy 27 to initiate deformation twinning comparing with Alloy 34 and lead to a higher density of twins at -196°C . In other words, by approaching the magnetic transition temperature, one expects a significant change in the GSFE driven by the change in the magnetic state.^[55]

5.3. Competitive Deformation Mechanisms

Dislocation slip and deformation twinning are two competitive mechanisms during deformation process of austenitic stainless steels.^[14,40,41,48] In AISI 316 steel with a nitrogen content of 0.04 wt%, it was found that deformation mainly occurs by dislocation in the beginning; deformation twinning occurs in the later stage of deformation with high deformation strain. In AISI 316 steel with a high nitrogen content (0.53 wt%), besides the above steps, second-order twinning occurs in the later stage of deformation.^[14] Similar phenomena have been observed in high nitrogen containing steel, Alloy 34, as shown in **Figure 5**. At low deformation strain (9 mm from the fracture surface), deformation is mainly by dislocation slip (white lines/points) with some deformation twins (red lines) (**Figure 5a**). With increasing deformation strain (3 mm from the fracture), more deformation twins can be observed (red lines in **Figure 5b**). With the ECCI image, multiple high order twinning has occurred with interactions between moving dislocations and twins (**Figure 5c**). With the

formation high order twins, the initial formed twin boundaries are not straight lines anymore due to the crystal rotation during deformation. These high ordered twins with other crystal orientations can intersect with the initial deformation twins as shown in **Figure 5c** and cause a deformation strengthening.

Deformation at cryogenic temperature has introduced dense twins in these two alloys. **Figure 6** shows the deformation microstructure in Alloy 34 tested at -196°C . These deformation twins initiated mainly at grain boundary and then propagated until they met another boundary (**Figure 6a**). From the ECCI image with high resolution, it can be found that there are dense nanotwins between the thick twin boundaries in the EBSD image (**Figure 6b**). With further increasing magnification (**Figure 6c**), it can be found that the distance between nanotwins is below 100 nm. Alloy 27 shows the similar twin microstructures. This indicates that dense nanotwins have initiated and developed in these two alloys tested at the cryogenic temperature, which lead to a TWIP phenomenon in the alloys. These images further show that the EBSD images cannot give a quantitative analysis of nanotwins in these two alloys.

In these two alloys, stacking faults have also been observed in both alloys as shown in **Figure 7**. Alloy 27 (**Figure 7a**) has wider and more stacking faults than Alloy 34 (**Figure 7b**). This may be due to the fact that Alloy 27 has a slightly lower stacking fault energy. Actually, formation of stacking faults and deformation twinning are a competitive process depending on local stress and crystal orientations.^[16,41] Deformation in the steels is a

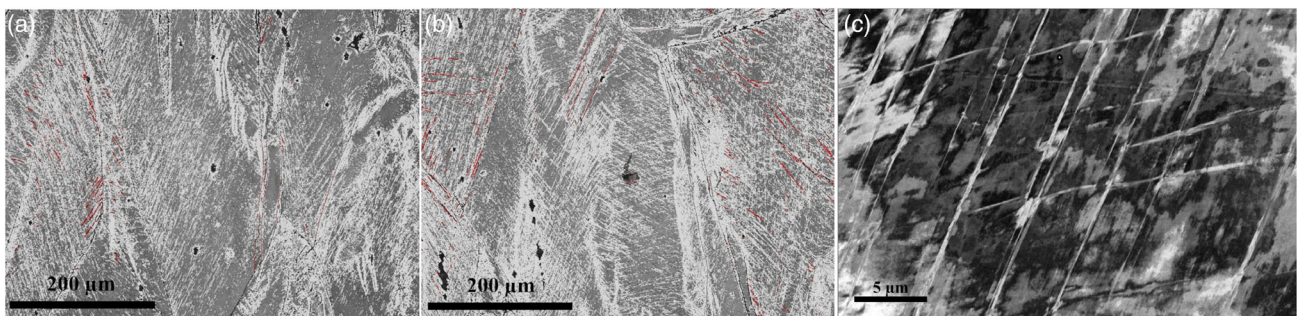


Figure 5. Deformation microstructures in Alloy 34 tested at RT, EBSD images/red lines: $\Sigma 3$ twin boundaries, white points/lines: low-angle grain boundaries $<10^{\circ}$, black lines: high-angle grain boundaries $\geq 10^{\circ}$, a) EBSD image taken 9 mm from the fracture surface, b) EBSD image taken 3 mm from the fracture surface, c) ECCI image taken 3 mm from the fracture surface showing high-order deformation twinning and its interaction with dislocations.

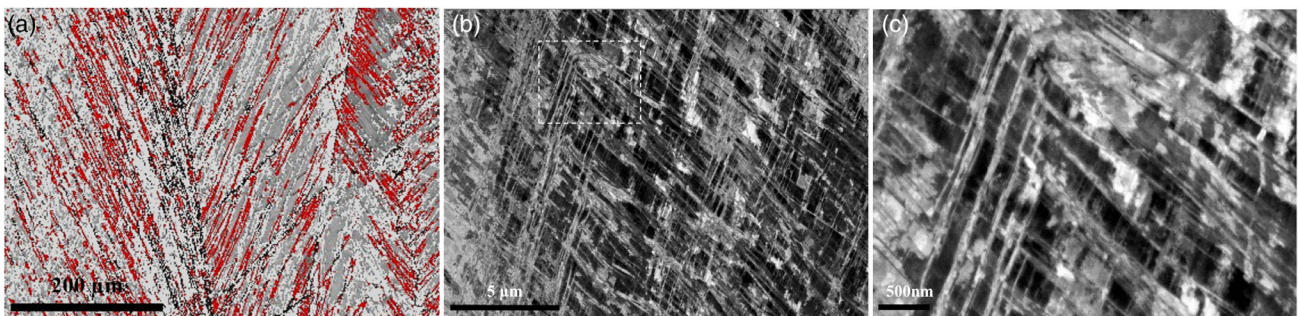


Figure 6. Deformation microstructures in Alloy 34 tested at -196°C , a) EBSD image taken 3 mm from the fracture surface, red lines: $\Sigma 3$ twin boundaries, white points/lines: low-angle grain boundaries $<10^{\circ}$, b) ECCI image taken 3 mm from the fracture surface, c) enlarged ECCI image (b) showing high-order deformation twinning and its interaction with dislocations.

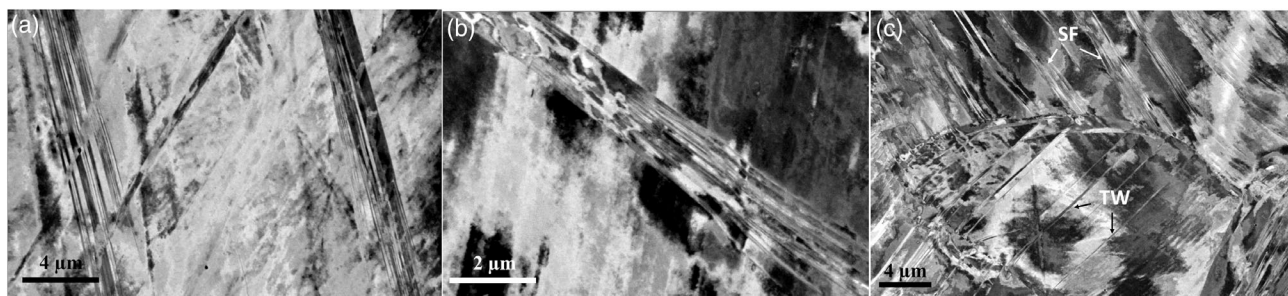


Figure 7. Formation of stacking faults and competitive growth of stacking fault (SF) and twin (TW), a) stacking fault observed in Alloy 27, b) stacking fault observed in Alloy 34, c) competitive growth of SF and TW in Alloy 27.

competitive process. Dislocation slip is dominant at low strain range, but formation of stacking fault and twinning become important in the later stage of deformation. This phenomenon has also been reported in other studies.^[13,20,50] At cryogenic temperature, it is mainly deformation twinning, but interaction between deformation twins and dislocation slip can still be observed, especially at local necking range. As known, formation of deformation twins can improve ductility and interaction between deformation twins and dislocation slip contributes a strengthening. This combination leads to a TWIP behavior of these steels at cryogenic temperature.

6. Conclusion

Influence of nitrogen on the deformation behavior and microstructure in two advanced austenitic stainless steels has been studied. The following conclusions can be obtained.

Addition of a high amount of nitrogen in the advanced stainless steels can significantly increase both strength and elongation at same time. This is the first report on this phenomenon in high Ni containing advanced austenitic stainless steels.

Addition of nitrogen promotes deformation twinning at room temperature, which is one mechanism for a high elongation of the steel. The increased twinning activity is mainly due to the increased flow stress and strain hardening rate in nitrogen steels, reaching the critical stress for twinning at smaller strain levels. Formation of stacking faults is another one besides dislocation slip. At cryogenic temperature, these advanced austenitic stainless steels show a TWIP effect.

Addition of nitrogen can cause a higher magnetic transition temperature compared to the low-nitrogen case. This significantly increases the stacking fault energy and consequently affects the deformation mechanism in the steels at cryogenic temperature.

Acknowledgements

This article is published by permission of Sandvik Materials Technology. The supports of Dr Tom Eriksson, Ms Eva Lindh-Ulmgren, and the assistances of ECCI study by Mr Jerry Lindqvist, lattice parameter and magnetic property by Drs Peter Svedlindh, Nazanin Hosseini, Esmat Dastanpour Hosseinabadi, and Mr Jan Andersson are gratefully acknowledged. L.V. and Z.D. acknowledge the Swedish Research Council (VR), the Swedish Foundation for Strategic Research (SSF), the Carl Tryggers

Foundations, and the Swedish Innovation Agency (VINNOVA). The computations were performed on resources provided by the Swedish National Infrastructure for Computing (SNIC) at Linköping.

Conflict of Interest

The authors declare no conflict of interest.

Data Availability Statement

The data that support the findings of this study are available from the corresponding author upon reasonable request.

Keywords

austenitic stainless steels, elongation, nitrogen, strengthening, twin induced plasticity

Received: April 30, 2022

Revised: July 15, 2022

Published online:

- [1] P. Marshall, *Austenitic Stainless Steels*, Elsevier Applied Science Publishers Ltd., London, **1984**.
- [2] R. R. Winston, *Uhlrig's Corrosion Handbook*, John Wiley & Sons, Inc., Hoboken, NJ **2011**, ISBN: 9780470080320, <https://doi.org/10.1002/9780470872864.ch51>.
- [3] S. Bernhardsson, *The stress corrosion cracking resistance of Sandvik Sanicro 28 in Aerated aqueous chloride solutions*, Sandvik lecture, S-52-77, **1985**.
- [4] P. Kangus, G. Chai, *Adv. Mater. Res.* **2013**, 794, 645.
- [5] M. O. Speidel, *Met. Trans. A*, **1981**, 12A, 779.
- [6] A. Svyazhin, L. Kaputkina, I. Smarygina, D. Kaputkin, *Steel Res. Int.* May, **2022**, 2200160, <https://doi.org/10.1002/srin.202200160>.
- [7] S. Li, C. Zhang, J. Lu, R. Chen, D. Chen, G. Cui, *Mater. Express* **2021**, 11, 1901.
- [8] J. W. Simmons, *Mater. Sci. Eng.* **1996**, A207, 159.
- [9] V. G. Gavriljuk, H. Berns, *High Nitrogen Steels*, Springer, Berlin **1999**, p. 1.
- [10] M. O. Speidel, *Materialwiss. Werkstofftech.* **2006**, 37 875.
- [11] M. L. Byrnes, M. Grujicic, W. S. Owen, *Acta Metall.* **1987**, 35, 1853.
- [12] G. I. Haddick, *The development of nickel-free austenitic stainless steels for ambient and cryogenic applications*, eScholarship, University of California, **2011**, edssch.oai:escholarship.org/ark:/13030/qt17c5d949.

- [13] M. Talha, C. K. Behera, O. P. Sinha, *Mater. Sci. Eng. C* **2013**, 33, 3563.
- [14] Mullner, et al., *Mater. Sci. Eng. A* **1993**, 164, 164.
- [15] R. E. Stoltz, J. B. van der Sande, *Met. Trans. IIA* **1980**, 1033.
- [16] V. G. Gavriljuk and S. E. Jephimenko, in: *Proc. 2nd Int. Conf. on High Nitrogen Steels HNS 90* (Eds: G. Stein, H. Witulski), Aachen, Diisseldorf, Germany **1990**, p. 11.
- [17] A. Das, *Metall. Mater. Trans. A* **2015**, 47, 748.
- [18] T.-H. Lee, C.-S. Oh, S.-J. Kim, S. Takaki, *Acta Mater.* **2007**, 55, 3649.
- [19] P. Milliner, C. Solenthaler, P. Uggowitzer, M. O. Speidel, *Mater. Sci. Eng.* **1993**, 164, 164.
- [20] D. Molnar, S. Lu, S. Hertzman, G. Engberg, L. Vitos, *Mater. Character.* **2020**, 170, 110726.
- [21] D. Hull, D. J. Bacon, *Dislocations*, Oxford University Press, New York **1989**.
- [22] S. Kubota, Y. Xia, Y. Tomota, *ISIJ Int.* **1998**, 38, 474.
- [23] J.-Y. Lee, Y. M. Koo, S. Lu, L. Vitos, S. K. Kwon, *Sci. Rep.* **2017**, 7, 11074.
- [24] I. Karaman, H. Sehitoglu, Y. Chumlyakov, H. Maier, *JOM* **2002**, 54, 31.
- [25] Y. Kawahara, et al., *ISIJ Int.* **2021**, 61, 1029.
- [26] Y. Uematsu, K. Hoshino, *Tetsu-to Hagane* **1983**, 69, 686.
- [27] Z. Dong, S. Schonecker, W. Li, S. K. Kwon, L. Vitos, *Int. J. Plast.* **2018**, 109, 43.
- [28] Z. Dong, S. Schonecker, D. Chen, W. Li, S. Long, L. Vitos, *Int. J. Plast.* **2019**, 119, 23.
- [29] L. Vitos, *Computational Quantum Mechanics For Materials Engineers: The EMT0 Method And Applications*, Springer, London **2007**.
- [30] L. Vitos, *Phys. Rev. B* **2001**, 64, 014107.
- [31] K. Kadas, L. Vitos, B. Johansson, J. Kollar, *Phys. Rev. B* **2007**, 75, 035132.
- [32] L. Vitos, H. L. Skriver, B. Johansson, J. Kollar, *Comput. Mater. Sci.* **2000**, 18, 24.
- [33] L. Vitos, I. A. Abrikosov, B. Johansson, *Phys. Rev. Lett.* **2001**, 87, 156401.
- [34] J. P. Perdew, K. Burke, M. Ernzerhof, *Phys. Rev. Lett.* **1996**, 77, 3865.
- [35] P. Soven, *Phys. Rev.* **1967**, 156, 809.
- [36] B. L. Györfy, *Phys. Rev.* **1972**, B5, 2382.
- [37] A. J. Pindor, J. Staunton, G. M. Stocks, H. Winter, *J. Phys. F: Met. Phys.* **1983**, 13 979.
- [38] J. Staunton, B. Györfy, A. Pindor, G. Stocks, H. Winter, *J. Magn. Magn. Mater.* **1984**, 45 15.
- [39] B. L. Györfy, A. J. Pindor, J. Staunton, G. M. Stocks, H. Winter, *J. Phys. F: Met. Phys.* **1985**, 15, 1337.
- [40] D. J. Dyson, B. Holmes, *J. Iron Steel Inst.* **1970**, 208, 469.
- [41] F. C. Hull, S. K. Hwang, J. M. Wells, R. I. Jaffee, *J. Mater. Eng.* **1987**, 9, 81.
- [42] A. K. Majumdar, P. V. Blanckenhagen, *Phys. Rev. B* **1984**, 29, 4079.
- [43] S. A. Kibey, J. B. Liu, D. D. Johnson, H. Sehitoglu, *Acta Mater.* **2007**, 55, 6843.
- [44] S. A. Kibey, L.-L. Wang, J. Liu, H. Johnson, H. Sehitoglu, D. D. Johnson, *Phys. Rev. B* **2009**, 79, 214202.
- [45] T. Cai, Z. J. Zhang, P. Zhang, J. B. Yang, Z. F. Zhang, *J. Appl. Phys.* **2014**, 116, 163512.
- [46] J. W. Christian, S. Mahajan, *Prog. Mater. Sci.* **1995**, 39, 1.
- [47] B. C. De Cooman, Y. Estrin, S. K. Kim, *Acta Mater.* **2018**, 142, 283.
- [48] M. A. Meyers, O. Vöhringer, V. A. Lubarda, *Acta Mater.* **2001**, 49, 4025.
- [49] K. M. Rahman, V. A. Vorontsov, D. Dye, *Acta Mater.* **2015**, 89, 247.
- [50] I. Gutierrez-Urrutia, S. Zaefferer, D. Raabe, *Mater. Sci. Eng. A* **2010**, 527, 3552.
- [51] S. A. Kibey, J. B. Liu, D. D. Johnson, H. Sehitoglu, *Acta Mater.* **2007**, 55, 6843.
- [52] S. Curtze, V.-T. Kuokkala, *Acta Mater.* **2010**, 58, 5129.
- [53] T. S. Byun, *Acta Mater.* **2003**, 51, 3063.
- [54] L. Bracke, L. Kestens, J. Penning, *Scr. Mater.* **2009**, 61, 220.
- [55] I. Bleskov, T. Hickel, J. Neugebauer, A. Ruban, *Phys. Rev. B* **2016**, 93, 214115.